Optimized Calibration Methodology of VIIRS Day-Night Band Low Gain Stage Using a Solar Diffuser

Junqiang Sun[1,2] and Menghua Wang[1]

[1]NOAA National Environmental Satellite, Data, and Information Service,
Center for Satellite Applications and Research, E/RA3,
5830 University Research Ct., College Park, MD 20740, USA

[2]Global Science and Technology, 7855 Walker Drive, Suite 200, Greenbelt, MD 20770, USA

Applied Optics

Submitted on 2/28/2017

ABSTRACT

An enhanced methodology of the standard on-orbit calibration of the day-night band (DNB) of the Visible Infrared Imaging Radiometer Suite (VIIRS) on-board the Suomi National Polar-orbiting Partnership (SNPP) satellite is presented, specifically for the low gain stage (LGS). The range of the "sweet spot" for the fully illuminated scans in the calibration events is expanded from 4^o to 7.8^o in order to increase the number of fully illuminated scans to 72, which then permits a complete calibration of the DNB to be carried out within one orbit for all 36 aggregated modes and the two mirror sides. This improves over the current operational methodology, which is with a more restricted range for the sweet spot that requires multiple orbits to complete a calibration. The expansion necessarily requires the expansion of a key calibration input, the product of the bidirectional reflectance factor (BRF) of the solar diffuser (SD) with the vignetting function (VF) describing the transmission of the attenuation screen in front of the SD port, or BVP for short. The expanded BVP is derived by fitting the function in three separate intervals and joining them smoothly to form a single function. Additional enhancements include the adaptation of the previously improved SD degradation and all other improvements developed for reflective solar bands from the previous work. The time-dependent relative spectral response (RSR) is also characterized and implemented, and its impact and improvements are studied and discussed. The result shows that the improved DNB calibration coefficients are more stable, smooth and less noisy.

Keywords: Remote sensing, VIIRS, Nighttime lights, Day-night band, Vis/NIR, Solar Diffuser, On-orbit

1. Introduction

Since its launch on 28 October 2011 more than five years ago, the Visible Infrared Imaging Radiometer Suite (VIIRS) on board the Suomi National Polar-orbiting Partnership (SNPP) satellite has been making global observation of Earth environment producing a wide range of science output [1,2]. Figure 1 is a schematic diagram of the VIIRS Instrument. Along with 14 reflective solar bands (RSBs) in the spectral range 0.41 to 2.25 μm and 7 thermal emissive bands (TEBs) in the spectral range 3.7 to 12.013 μm, panchromatic day-night band (DNB) is a unique band covering the spectral range 0.5 to 0.9 μm designed for the observation of night scenes. The VIIRS DNB improves over its predecessors such as DMSP-OLS [3-5] with much finer spatial and temporal resolution as well as radiometric sensitivity [6,7]. It covers a wide dynamic range, spanning over seven orders of magnitude, through operation in three gain settings – the low gain stage (LGS), the medium gain stage (MGS) and the high gain stage (HGS) [8-15].

The on-orbit calibration on the DNB also goes through the built-in solar diffuser (SD) panel, shown in Fig. 1, similarly as the RSBs [8,10]. Although the MGS and the HGS saturate during calibration events and therefore cannot directly utilize SD calibration data, the LGS can still operate within its range to achieve successful calibration. Provided that the LGS is properly calibrated, the two higher gain stages then can be calibrated by referencing to the LGS via a ratio-based methodology [8,10,13].

Nevertheless, DNB is inherently a much more complex built and follows a more convoluted operation and data processing strategy, and therefore its calibration approach has been adjusted and enhanced accordingly [8]. A major operational adjustment for DNB calibration is the requirement of acquiring data over multiple consecutive orbits in order to complete an equivalent SD-based calibration [8, 10]. In the current methodology, within the interval of full-illumination of SD during a calibration event, when the spacecraft crosses the terminator in each orbit, only about 38 scans within a pre-defined "sweet spot" interval are selected for computation. Because the high number of aggregation modes of data acquisition for the DNB, the number of scans within the "sweet spot" cannot meet the required number per complete calibration in just one orbit. The standard "sweet spot" is adequate to provide for a complete calibration of RSBs within one orbit, but falls short for the DNB. The current operational strategy for DNB calibration is to gather data from the "sweet spot" over one day to generate a daily average [8,10].

This work examines the calibration methodology for the LGS of the DNB, and examines among numerous possible improvements the expansion of the "sweet spot" that can permit a complete calibration within one orbit. The expansion of "sweet spot" is equivalent to the expansion of the angular range of the light impinging on the SD [16], and necessarily forces the reconsideration of the bidirectional reflectance factor (BRF) of the SD and the vignetting function (VF) characterizing the transmission of the attenuation screen in front of the SD port [17,18]. Specifically, it is the product of the BRF and the VF that will be expanded and re-derived. The product is abbreviated as BVP, short for BRF-VF product, as in our previous work [17] and the abbreviation will be used in the context of this work as well. The time-dependent relative spectral response (RSR) [16,19] is also studied, characterized and applied. The improvement in the F-factors from the application of the time-dependent RSRs is shown by comparing with the performance result using the pre-launch RSR [20]. Finally, the on-orbit change of the reflectance of the SD, the SD-degradation or H-factor, is another crucial component of the calibration pipeline to be considered [21-23]. However, the H-factor has already been improved in previous work [22] and is an independent factor not affected by the change of the "sweet spot" range. This work simply adopts the already-improved H-factor into DNB calibration. Since the improved H-factor is more stable and smooth [22], this update alone already improves the result of the DNB calibration. The final result will show that the DNB calibration coefficients, or its F-factor, are improved by having better inputs and more data.

The rest of the paper is presented as follows. Section 2 covers the DNB calibration methodology and the details of the improvements. Section 3 presents the improved results in DNB F-factors and some brief discussions. Section 4 summarizes and concludes.

2. Calibration Methodology

A. SD Observation Profile and "Sweet Spot"

The VIIRS SD, made of specially manufactured Spectralon with near Lambertian reflectance property, is installed inside of the VIIRS instrument primarily to serve the on-orbit calibration of the RSBs [16]. For the purpose of preventing saturation of the RSBs, a screen is placed in front of the SD port, as shown in Fig. 2, to attenuate the incoming solar illumination. The calibration of RSBs using the SD can take place only during a short window of time in each orbit, within which the SD is fully illuminated, when the satellite crosses the terminator from the nightside to the dayside of the Earth [16]. Figure 3 shows the background-subtracted instrument response digital count, denoted as *dn*, for SNPP VIIRS Band M6 as a function of solar declination angle in the instrument coordinate system for a time interval covering the full illumination of the SD. The solar declination angle, starting from the nightside at a positive angle, decreases with time at a rate of about 3.6° per minute and reaches zero when the instrument is at the terminator [16]. Full illumination occurs in the solar-angle range from 5° to

19°, corresponding to a time period of about 4 minutes. The response increases with the declination angle, as shown in the full illumination curve in Fig. 3, because of the angle dependence of the BRF of the SD and that of the VF of the SD screen [17,18]. In principle, any data from the RSB observation of the SD within the full-illumination range can be used to derive the RSB calibration coefficients, or F-factors. The selection of the solar declination angle range of 13° to 17° proper for VIIRS RSB SD calibration [16], the so called “sweet spot”, is made by considering the number of the data samples, the difficulty of the viewing geometric effect correction for larger angle, and the expectation of high signal-to-noise ratio (SNR). The declination angle range of 14° to 18° has also been chosen as the “sweet spot” by others [8]. About 38 scans are available from the “sweet spot” during full illumination, and provide an adequate dataset for the derivation of the RSB F-factors [16]. Similarly, any data of SD observation by DNB within the full-illumination range can be used to calibrate the DNB and to derive the calibration coefficients, F-factors, as long as its detectors are not saturated. A key point to make explicitly here is that the “sweet spot” for DNB SD calibration does not need to be the same as that for the RSB, and in fact this work makes use of this flexibility to expand the range.

VIIRS DNB is composed of four charge-coupled device (CCD) detector arrays [8]. The detectors are called “subpixel” for DNB because observations from many detectors are used to construct an equivalent result of a single pixel. Among the four arrays, two are for HGS, one for MGS, and one for LGS [8]. There are 672 subpixel detectors along-track in all four arrays, while there are 250, 3, and 1 subpixel detectors along-scan in each of the two arrays for the HGS, the array for the MGS, and the array for the LGS, respectively. The 672 subpixel detectors along-track for each subpixel along scan are aggregated on-board to create 16 pixels with a size of near-constant 742 m along-track [8]. The 16 aggregated pixels are also commonly referred to as the “aggregated detectors”. The subpixels along-scan for each aggregated detector in a given gain status are further aggregated with a time-delay-integration (TDI) scheme. The two arrays for HGS have the highest sensitivity, the array for MGS has a sensitivity two orders of magnitude lower than those of HGS detector arrays, and the one for LGS has a sensitivity further lower by three orders of magnitude [8].

In the SD view sector, all the responses of the 16 aggregated detectors are collected for all four detector arrays. During the full-illumination time period interval, the aggregated detectors for both the HGS and MGS are all saturated and thus no data collection can be used for calibration using the SD as a reference [8,10]. However, the aggregated detectors of the LGS are not saturated and their data can be used for calibration using the SD reference in a similar way as the RSBs although with some slight procedural differences. This analysis focuses on the SD calibration of the VIIRS DNB with gain stage LGS.

In order to achieve similar spatial size for each pixel in the observation of Earth surface, the DNB Earth view (EV) is divided into 64 aggregation zones, which then are grouped into 32 pairs [8]. The two zones in each pair are mirrored with respect to the nadir. The DNB with LGS has 32 different aggregation modes, each of which is applied to a corresponding pair of aggregation zones. For different aggregation modes, the sampling time intervals are different. Thus, the gains of 32 aggregation modes are different and require separate calibration for each mode. Separate calibration is also needed for each of the 16 aggregated detectors and for each of the two sides of the half-angle mirror (HAM) [8,10]. Thus there are a total of 1024 calibration coefficients for VIIRS DNB with LGS.

In the VIIRS SD view sector, 36 aggregation modes are implemented and programmed, with 32 for EV observation and 4 for testing purpose [8]. In every two contiguous scans, the SD view stays with a unique aggregation mode and then switches to the next aggregation mode along the aggregation mode sequence. To cover the all 36 aggregation modes and two sides of the HAM, 72 scans are needed, which spans approximately 7.8^{o} in declination angle. As shown in Fig. 3 and discussed previously, the full-illumination range during a SD calibration event spans over a range of about 14^o, from 5^o to 19^o, which is larger than the required 7.8^o range. This makes it possible to select a "sweet spot" within this range for the calibration of DNB to cover all 36 modes and two sides of the HAM. Following the same consideration as for the RSBs [16], we can select the declination angle range from 10.2^o to 18^o as the "sweet spot" for the DNB. Occasionally with this expanded "sweet spot" there will be a few more scans than the needed 72, and for such cases the 72 scans with the largest declination angles within the "sweet spot" are selected for the DNB LGS SD calibration. Figure 4 shows the DNB LGS Detector 1 background subtracted instrument response. Same as the case for the RSBs, the background of the DNB is provided by the space view (SV), where the aggregation mode of the DNB will be the same as for the SD sector. In other words, the SV and the SD sectors will be seen by the DNB in the same aggregation mode in each scan. Figure 5 shows the aggregation mode numbers for the corresponding scans shown in Fig. 4. It is clearly seen from Figs. 4 and 5 that the DNB instrument response strongly depends on the aggregation mode. With the scans in the new "sweet spot", calibration coefficients can be derived for each aggregation mode, HAM side, and detector for the DNB LGS from the SD measurement of each orbit. It is worth to mention again that the "sweet spot" used in this analysis has been expanded from those used in literatures [8,10], where the "sweet spot" covers the declination angle range of 14° to 18°, which is also the designed parameter specified in the VIIRS calibration ATBD for the DNB [8]. Because this standard "sweet spot" is of a smaller range, multiple calibrations events (orbits) are needed to derive a set of the DNB calibration coefficients from the SD observations.

B. SD Calibration Algorithm

When the SD is fully illuminated by the Sun through the SD port, the scattered sunlight radiance from the SD to the DNB can be expressed as

$$L_{DNB}(t) = \frac{\tau_{SDS}\cos(\theta_{SD})}{d_{ES}^2}\frac{\int L_{Sun}(\lambda)BRF_{SD,RTA}(\lambda,t)RSR_{DNB}(\lambda,t)d\lambda}{\int RSR_{DNB}(\lambda,t)d\lambda}, \tag{1}$$

where τ_{SDS} is the VF of the SD screen placed in the front of the SD port, d_{ES} is the Earth-Sun distance in Astronomical Unit (AU), θ_{SD} is the solar-zenith angle to the SD, $L_{Sun}(\lambda)$ is the solar radiance at the Earth-Sun distance of one AU, $BRF_{SD,RTA}(\lambda,t)$ is the BRF of the SD for the view direction from the rotating telescope assembly (RTA) to the SD at wavelength λ and time t, and $RSR_{DNB}(\lambda,t)$ is the detector-averaged RSR of the DNB at time t. The BRF, $BRF_{SD,RTA}(\lambda,t)$, changes on-orbit with time. It is inherently assumed that the SD degradation with respect to incident and outgoing directions is uniform, and so the time and angle dependence of the BRF can be separated into the form

$$BRF_{SD,RTA}(\lambda,t) = \rho_{SD,RTA}(\lambda)H(\lambda,t)\,, \qquad (2)$$

where $\rho_{SD,RTA}(\lambda)$ is the BRF before launch with outgoing direction toward the RTA for the wavelength λ [24] and $H(\lambda,t)$ is SD degradation factor at the given wavelength, which can be derived from the regular scheduled SD stability monitor (SDSM) calibration, since prelaunch BRF measurement [21-23]. Both $BRF_{SD,RTA}(\lambda,t)$ and $\rho_{SD,RTA}(\lambda)$ are functions of the incident direction of incident light. However, recent investigations have shown that SD does not degrades uniformly with respect to the incident and outgoing directions [25]. Nevertheless, the purpose of this work is to demonstrate the optimized methodology, and the issue of the SD degradation bias will not be addressed here.

For SNPP VIIRS DNB, the at-aperture radiance L and the background-subtracted instrument response dn is characterized by a linear relationship of the following form [8]:

$$L_{DNB}(Sample, Scan, D, t) = \frac{F_G(D,M,A,t)dn_{DNB,G}(Sample, Scan, D)}{RVS_{DNB}(\vartheta, M)}\,, \qquad (3)$$

where A is the number of the aggregation mode, $Sample$ is the pixel number along the scan direction, $Scan$ is the scan number along track direction, D is the detector number of the gain stage G, $L_{DNB}(Sample,Scan,D,t)$ is the radiance at the sample of the scan observed at time t by the detector D, M is the side number of the instrument HAM at the scan, and G is the gain stage of the detector D at the sample of the scan. $RVS_{DNB}(\vartheta,M)$ is the response-versus-scan-angle (RVS) of the DNB at the angle of incidence (AOI), ϑ, of the HAM M, which is a function of the sample and measured prelaunch. $F_G(D,M,A,t)$ is the calibration coefficient, the F-factor, for detector D of the gain stage G, HAM side M with aggregation mode A at time t, which is inversely proportional to the on-orbit gain change, and the term $dn_{DNB,G}(Sample,Scan,D)$ is the background-subtracted instrument response of detector D of gain stage G.

Equation (3) can be applied to SD view for DNB LGS and also Eqs. (1), (2) and (3) can be combined to obtain

$$F_{LGS}(D,M,A,t)=\frac{RVS_{DNB}(\vartheta_{SD},M)\cos(\theta_{SD})\int L_{Sun}(\lambda)\tau_{SDS}\rho_{SD,RTA}(\lambda)H(\lambda,t)RSR_{DNB}(\lambda,t)d\lambda}{d_{ES}^{2}dn_{DNB,LGS,SD}(A,D)\int RSR_{DNB}(\lambda,t)d\lambda}, \quad (4)$$

where ϑ_{SD} is the AOI of the HAM for the SD view and $dn_{DNB,LGS,SD}(A,D)$ is the background-subtracted instrument response of the DNB LGS detector D with aggregation mode A. In SD sector, there are 16 samples for the LGS along-scan and $dn_{DNB,LGS,SD}(A,D)$ is the average of the 16 samples. Because occasionally there are more than 72 scans in the sweet spot, the 72 scans of the highest responses are selected to match all 72 aggregation modes and HAM sides in the sweet spot.

C. Main Inputs

The first main input into to calibration computation to reconsider is the VF of the SDS, τ_{SDS}, and the BRF, $\rho_{SD,RTA}(\lambda)$, of the SD. Both functions depend on two independent solar angles [17] such as solar declination, solar azimuth or any two independently selected solar angles in any selected coordinate system. Their dependences on the solar angles were measured prelaunch but with the solar elevation angle range restricted within [14^o, 18.5^o], which is smaller than the "sweet spot" selected in this analysis and as discussed above. For the BRF, the prelaunch measurements were implemented at selected wavelengths and linear interpolation is used to obtain the BRF at other wavelengths [24]. As seen in Eq. (4), only the product of the SD BRF and the SDS VF or BVP, $\tau_{SDS}\times\rho_{SD,RTA}(\lambda)$, is actually needed to derive the F-factors from SD observations [17]. It is worth to mention that the BVP cannot be derived from the yaw measurements of the DNB since the aggregation mode switches every two scans [8]. Of course, the derivation of the BVP is possible if the aggregation mode is fixed during the entire yaw measurements.

The relative dependence of the BVP on the incident angles can be derived, using the on-orbit measurements of the RSBs from the planned yaw maneuvers, at each wavelength of the RSBs [17]. To re-derive BVP to cover the expanded “sweet spot” angular range from 10.2^o to 18^o, the relative BVP from the yaw data of the RSBs, measured at each respective wavelength of the RSBs, are first derived in each of three different but overlapping ranges of the declination angles, [10.2^o, 14.2^o], [12.1^o, 16.1^o], and [14^o, 18^o]. The procedure fits the measured data to two-dimensional quadratic forms and then by smoothly connects the three quadratic forms in the overlapping regions. The relative BVP at other wavelengths is obtained by linearly interpolating between the wavelengths of the RSBs. Finally, the absolute BVP is obtained by matching the derived relative BVP with prelaunch results in the declination range of the prelaunch measurements. This expanded absolute BVP is applied in this improved computation of DNB calibration. Figure 6 shows the derived BVP from the yaw measurements of Band M6 (745 nm), which smoothly varies with both the solar azimuth and declination angles in the instrument coordinate system.

The RSR, $RSR_{BD}(\lambda,t)$, may change on-orbit especially when the out-of-band (OOB) RSR contribution is large, as is the case for Band M1, or that the band width is very large as the case in DNB. The RSR on-orbit changes can be induced by the degradation of the instrument’s optical system, the degradation of the detectors, and other possibilities. If the degradation of optical system is the main cause for the on-orbit changes of the SNPP VIIRS RSBs, they can be derived from the time-dependent F-factors of the RSB [16,19]. The wavelengths of the RSBs are listed in Table 2. The same approach as applied to derive the time-dependent RSR for SNPP VIIRS RSBs [16] can be applied here to calculate the time-dependent RSR, $RSR_{BD}(\lambda,t)$ in Eq. (4), for the DNB using the F-factors of the RSBs and the prelaunch measured RSR of the DNB.

Figure 7 shows the time-dependent RSR for the DNB. There are four sets of RSR in the figure, one measured at prelaunch and other three for the times on March 20, 2012, August 2, 2013, and January 25, 2015. From Fig. 7, it can be seen that VIIRS DNB has a bandwidth larger than 400 nm and covers the spectrum range of bands M4-M7. Due to the faster degradation of the RTA in the near-infrared (NIR) spectral region, the RSR of the DNB decreases with time at long wavelength range while increases in the short wavelength range. It can also be seen that the RSR changes comparatively larger in the early mission and becomes almost negligible after three years on-orbit, as displayed by the two curves of “08/02/2013” and “01/25/2015” being nearly indistinguishable. This is due to the slowdown of the gain degradations of the NIR and SWIR bands. In this analysis, the time-dependent RSR of the DNB is applied in Eq. (4) to calculate the F-factors of the DNB LGS. The impact of the time-dependent RSR on the F-factors derived from the SD calibration for the DNB will be assessed in Section 3.

The SD degradation or H-factor, $H(\lambda,t)$, is computed from regularly scheduled SDSM measurements at eight wavelengths, which are listed in Table 2. The key improvement analysis has already been completed previously [22] and a brief description is provided. Figure 8 shows the SD degradation at the wavelengths of the eight SDSM detectors. Symbols in the figure are directly measured values. The SD degradation is strongly wavelength dependent and degrades much faster at shorter wavelengths. They change smoothly with respect to the wavelengths except for SDSM detectors D7 and D8, shown by the two top curves in Fig. 8, which have greater noise. For reduction of the noise in detectors D7 and D8, their SD measured degradations are fitted to exponential functions of time. The solid lines, the fitted SD degradations for D7 and D8 and the direct linear connections of measure data for other six detectors D1-D6, in the figure are used in this analysis. The SD degradations in Fig. 8 have been normalized at the time of launch, October 28, 2011. The SD degradation at a wavelength between two adjacent SDSM wavelengths is linearly interpolated. For the DNB, only the SD degradations measured by the SDSM detectors D3-D8 are needed to cover the spectral range of the DNB, shown in Fig. 7. Recent investigations have unraveled an effect, dubbed the “SD-degradation non-uniformity effect”, or the anisotropic angular dependence in the degradation of SD, that generates an inherent error into the RSB calibration pipeline. The bias is especially apparent when lunar-based calibration result is compared with SD-based calibration result. This long-standing issue has been resolved for RSB calibration. This is also an issue be addressed for DNB calibration using SD but does not fall within the scope of this work, and therefore will be addressed separately.

3. DNB LGS Calibration Coefficients and Performance

SNPP VIIRS was turned on after being on orbit for 11 days on November 8, 2011. Same as the RSBs, the DNB views the SD in every scan and the SD is fully illuminated whenever it crosses the Earth terminator from the nightside to the dayside at the South Pole. Its SD calibration, also similar to the RSBs, is automatically performed in every orbit for every detector, HAM side, and aggregation mode of the SNPP VIIRS DNB LGS. A set of 1024 F-factors is generated per orbit and results in about 14 sets of F-factors per day, using the optimized methodology described in Section 2. On the other hand, the current operational method generates only half as much for the daily production [8,10]. In this section, the F-factors for the DNB LGS are derived from the SD observations using the optimized methodology. The improvements of the results are shown and discussed.

Figure 9 shows the F-factors derived from the SD observations on 1 February 2016 for DNB LGS Detector 1 HAM 1 Aggregation Modes 1 and 14. The blue symbols, filled triangles for Mode 1 and diamonds for Mode 14, are the new results derived from the optimized methodology described in Section 2. The important outcome to note is that the new methodology, as expected, generates a F-factor for every orbit to give a total of 14 F-factors for the day, as demonstrated by each of the two aggregation modes in the plot. For each mode, the declination angle of the scan varies with orbit. The declination angles for different modes in each orbit are also different. The declination angle for each mode in each orbit in fact can be precisely determined. In Fig. 9, the green symbols, empty squares for Mode 1 and squares with cross for Mode 14, are the results derived from the current operational methodology. Also as expected, there are only 8 and 7 green symbols, instead of 14, F-factors for Aggregation Modes 1 and 14, respectively. As seen in Fig. 9, not only the numbers of F-factors from the operational method are different, but also their trends over the orbits are different. In principle, the F-factors within each mode should remain about the same over the course of a day since significant change of the instrument performance is not expected during a day of normal operation. However, it can be seen that each set of F-factors fluctuates with an uncertainty of ~1% over the course of a day due to various calibration errors and instrument noises. Nevertheless, the comparison of solid blue lines and dashed green lines clearly demonstrates that the F-factors derived using the extended “sweet spot” are not noisier than those in the original narrow “sweet spot”. This is a direct justification for the extension of the “sweet spot” described in Section 2.

Figure 10 shows the F-factors, normalized at the first measurement, for DNB LGS Detector 1 Aggregation Mode 1 for the entire mission. The green triangles are the F-factors derived from data of each individual orbit while the red diamonds are the daily averaged values. A fluctuation of about 2% in the derived F-factors is clearly seen in Fig. 10, and this variation is about a magnitude larger than that in the F-factors of the RSBs derived with the same SD observations. This is understandable because there are about 10 (or 20) scans of data for a dual (or single) band and 48 samples in each scan for a RSB F-factor, while there is one scan of data and 16 samples in the scan for a DNB F-factor. The daily averaging reduces the fluctuation by at least a factor of 3 to make the F-factors much more stable, with variation within ±0.3%. From Fig. 10, it is also seen that the F-factors have increased about 21.5% in the past five years since VIIRS launch.

Figure 11 shows the F-factors for DNB LGS HAM Side 1 Detector 1 Aggregation Mode 32. Same as for Mode 1 in Fig. 10, green triangles are the F-factors derived from data of each individual orbit, while red diamonds are the daily averaged values of the F-factors. The F-factors have increased about 22.0% since launch, about same amount for Aggregation Mode 1. It can be clearly seen by comparing Figs. 10 and 11 that the fluctuation in the F-factors of Aggregation Mode 32 is 2.5 times larger than that in the F-factors of Aggregation Mode 1. The larger fluctuation in the F-factors of Aggregation Mode 32 is mainly due to the reduction of the collection time for each sample (smaller *dn* and smaller SNR), which is determined by the scan angle range per sample (see Table 1). In fact, the fluctuation in the F-factors derived from the data of each individual orbit increase with the aggregation mode with Mode 1 having the smallest and Mode 32 having the largest. This is consistent with data collection times, which can be derived from the data in Table 1. In other words, the larger data collection time for each sample the smaller is the fluctuation in the derived F-factors. Same as for the Aggregation Mode 1, the fluctuation in the F-factors of the Mode 32 is reduced by a factor of 3 after the daily averaging. The reduction of fluctuation by a factor of ~3 due to the daily averaging is also true for all other aggregation modes.

Figure 12 shows the daily-averaged F-factors of HAM Side 1 Detector 1 for all aggregation modes for the entire mission. The F-factors in Fig. 12 are normalized at the first measurement of the Aggregation Mode 1. They all increase smoothly with time. Comparing to those reported in literature [10], the F-factors displayed in Fig. 12 are much more smooth and stable, and have less noise. It is also seen in Fig. 12 that any seasonal oscillations, as typical in other and earlier results, have been removed. This is due to the adaptation of the previously improved SD degradation [22] and all other improvements developed for RSB in our previous studies [16], as well as the increase of the numbers of F-factors coming from the expansion of the "sweet spot" to allow every orbit to generate a complete set of F-factors. The F-factors are strongly aggregation-mode dependent due to the differences of the data collection time. The Aggregation Mode 1 has the largest data collection time for each sample and thus has the largest gain, resulting in the smallest F-factor for a given calibration event. Since the gain and the F-factor are inversely proportional to each other, and that data collection times decrease with aggregation mode number to give smaller gains, the F-factors then increase with the number as shown in Fig. 12.

Figure 13 shows the F-factors normalized at the first measurement for HAM side 1 detector 1 of all aggregation modes for comparison. It is seen in Fig. 13 that the F-factors for all aggregation modes perform consistently, increasing with time at about the same rate for a given time as expected since the main differences among the modes are the differences of their data collection times. Nevertheless, evidence of differences among the F-factors of the 32 aggregation modes are seen and the differences increase with time, reaching ~4% after five years on orbit. The simple explanation that the data collection times among the 32 aggregation modes smoothly increase with time seems contrived and cannot be verified. In any case, the root cause for the differences and their increase of is not known and further investigation is beyond the scope of this analysis.

Figure 14 displays the detector differences of the F-factors for HAM Side 1 Aggregation Mode 1. There are clear differences among the 16 detectors and the differences can be as large as 3.7%. However, the differences are very stable within 0.2% variations. Same as Aggregation Mode 1, stable detector differences of the F-factors are observed in all aggregation modes. Figure 15 shows the detector differences, averaged over time, for all 32 aggregation modes. The differences are strongly dependent on aggregation-mode. For most aggregation modes, the differences are within ~4% and can be simply described by a linear function of detector number. But there are aggregation modes for which the detector differences are larger and randomly vary with detector number, as seen in Fig. 15.

Figure 16 shows the HAM side ratios for the F-factors for all aggregation modes. The ratios for Aggregation Mode 1 are very stable. There is no long-term trend observed and the fluctuation of the ratios is less than 0.2%. There are no long-term trends observed in the ratios of all other aggregation modes as well even though the fluctuations become larger with the increase of the aggregation mode number. This is understandable since the F-factors become noisier with the number of the aggregation mode due to the reduction of the data collection time as previously discussed. In brief, the two HAM sides change with time with about the same rate according to the ratios shown in Fig. 16. This is consistent with the finding obtained from the RSB F-factors.

As discussed in Section 2, the RSR for SNPP VIIRS DNB has changed significantly in last five years after VIIRS launch. The time-dependent RSR has been applied in the SD calibration to derive the F-factors for the DNB as mentioned previously and thus the effect of the RSR on-orbit change has been mitigated in the F-factors shown in all figures in this section. Although mitigated, the impact of the RSR on-orbit change on the derived F-factors is still of interest to study. Figure 17 shows the ratios of the F-factors derived with time-dependent RSR applied and those derived with prelaunch measured RSR used for entire mission. Since both time-dependent and prelaunch RSRs are aggregation mode independent, the ratios of the two sets of the F-factors are same for all 32 aggregation modes. Thus, there is one curve in Fig. 17, which shows that the RSR on-orbit change has significant impact on the F-factors in early mission but the impact reaches its peak after two years on orbit. It brings about 2.5% error in the F-factors derived from the SD calibration for SNPP VIIRS DNB LGS if the effect of the RSR on-orbit change is not mitigated.

The overall result clearly demonstrates the success and the superiority of the optimized methodology for the aspects presented. There remain other key issues to be addressed. One of such issues, as already mentioned, is the impact of the non-ideal SD degradation behavior, dubbed “the SD degradation non-uniformity effect” [25], or the non-ideal anisotropic behavior that generates an inherent long-term bias in SD degradation and then in the calibration coefficients, F-factors. For the RSBs, the long-term bias has been mitigated by a hybrid methodology [26], which properly combines the SD [16] and lunar calibration results [27]. For DNB, these issues are to be investigated in future studies.

4. Summary and Conclusions

An enhanced methodology of the standard on-orbit calibration of the SNPP VIIRS DNB using SD is developed and described, enabling a complete DNB calibration within one orbit and significantly improving over the current methodology. The calibration coefficients for the DNB LGS are derived from the SD observations using the new methodology. It is shown that the improved coefficients are more stable, smooth and less noisy. In addition to the methodology improvement, the previously improved SD degradation and all other improvements developed for reflective solar bands from our previous studies are also adapted in the DNB SD calibration. The impact of the OOB contribution of the RSR is applied and its impact on the calibration coefficients is also discussed. Furthermore, the methodology developed in this analysis can be directly applied to all follow-on VIIRS instruments.

Acknowledgments

We would like to thank Mike Chu for bring to attention the importance of this topic. The views, opinions, and findings contained in this paper are those of the authors and should not be construed as an official NOAA or U.S. Government position, policy, or decision.

References

1. C. Cao, F. Deluccia, X. Xiong, R. Wolfe, and F. Weng, "Early on-orbit performance of the Visible Infrared Imaging Radiometer Suite (VIIRS) onboard the Suomi National Polar-orbiting Partnership (S-NPP) satellite," IEEE Trans. Geosci. Remote Sens., 52, 1142–1156, 2014.
2. X. Xiong, J. Butler, K. Chiang, B. Efremova, J. Fulbright, N. Lei, J. McIntire, H. Oudrari, J. Sun, Z. Wang, and A. Wu, "VIIRS on-orbit calibration methodology and performance," J. Geophys. Res. Atmos., 119, 5065–5078, 2014.
3. D. B. Johnson, P. Flament, and R.L. Bernstein, "High Resolution Satellite Imagery for Mesoscale Meteorological Studies", Bull. Amer. Met. Soc., 75, 5-33, 1994.
4. C. D. Elvidge, K. E. Baugh, E. A. Kihn, H. W. Kroehl, E. R Davis, "Mapping of City Lights Using DMSP Operational Linescan System Data", Photogrammetric Engineering and Remote Sensing, 63, 727-734, 1997.
5. C. D. Elvidge, K. E. Baugh, E. A. Kihn, H. W. Kroehl, E. R. Davis, "Relation between satellite observed visible-near infrared emissions, population, and energy consumption", Int. J. Remote Sens., 18, 1373–1379, 1997.
6. K. Southwell, "Night lights", Nature, 390, 1997.

7. C. D. Elvidge, K. E. Baugh, M. Zhizhi, F. –C. Hsu, “Why VIIRS data are superior to DMSP for mapping nighttime lights”, Proc. Asia Pac. Adv. Netw., 35, 62–19, 2013.
8. S. Mills, “VIIRS Radiometric Calibration Algorithm Theoretical Basis Document”, Doc. No.: D43777, Northrop Grumman Aerospace Systems: Redondo Beach, CA, USA, 2010.
9. S. D. Miller, S. P. Mills, C. D. Elvidge, D. T. Lindsey, T. F. Lee, J. D. Hawkins, “Suomi satellite brings to light a unique frontier of nighttime environmental sensing capabilities”, Proc. Nat. Acad. Sci., 109, 15707–15710, 2012.
10. J. Geis, C. Florio, D. Moyer, K. Rausch, F. J. De Luccia, “VIIRS Day-Night Band Gain and Offset Determination and Performance”, Proc. SPIE, 8510, 851012, 2012.
11. S. Mills, S. Weiss, K. Liang, “VIIRS day/night band (DNB) stray light characterization and correction”, Proc. SPIE, 8866, 88661P, 2013.
12. L. B. Liao, S. Weiss, S. Mills, B. Hauss, “Suomi NPP VIIRS day-night band on-orbit performance”, J. Geophys. Res. Atmos., 118, 12707–12718, 2013.
13. S. Lee, J. McIntire, H. Oudrari, T. Schwarting, X. Xiong, “A new method for Suomi-NPP VIIRS day-night band on-orbit radiometric calibration”, IEEE Trans. Geosci. Remote Sens., 53, 324–334, 2015.
14. S. Lee, K. F. Chiang, X. Xiong, C. Sun, A. Samuel, “The S-SNPP VIIRS day-night band on-orbit calibration/characterization and current state of SDR products”, Remote Sens., 6, 12427–12446, 2014.
15. S. Mills, S. D. Miller, “VIIRS Day-Night Band (DNB) calibration methods for improved uniformity”, Proc. SPIE, 9218, 921809, 2014.
16. J. Sun and M. Wang, “ On-orbit calibration of Visible Infrared Imaging Radiometer Suite reflective solar bands and its challenges using a solar diffuser “, Appl Opt., 7210-7223, 2015.
17. J. Sun and M. Wang, “On-orbit characterization of the VIIRS solar diffuser and solar diffuser screen," Appl. Opt., 54, 236-252, 2015.

18. J. McIntire, D. Moyer, B. Efremova, H. Oudrari, and X. Xiong, “On-orbit characterization of S-NPP VIIRS transmission functions,” IEEE Trans. Geosci. Remote Sens., 53, 2354–2892, 2015.
19. N. Lei, X. Xiong, B. Guenther, “Modeling the Detector Radiometric Gains of the Suomi NPP VIIRS Reflective Solar Bands”, IEEE Trans. Geosci. Remote Sens., 53, 1565-1573, 2015.
20. C. Moeller, J. McIntire, T. Schwarting, D. Moyer, and J. Costa, “Suomi NPP VIIRS spectral characterization: understanding multiple RSR releases,” Proc. SPIE 8510, 85101S, 2012.
21. E. Hass, D. Moyer, F. DeLuccia, K. Rausch, and J. Fulbright, “VIIRS solar diffuser bidirectional reflectance distribution function (BRDF) degradation factor operational trending and update,” Proc. SPIE, 8510, 851016, 2012.
22. J. Sun, M. Wang, “Visible Infrared Imaging Radiometer Suite solar diffuser calibration and its challenges using a solar diffuser stability monitor”, Appl. Opt., 53, 8571-8584, 2014
23. J. Fulbright, N. Lei, B. Efremova, X. Xiong, “Suomi-NPP VIIRS Solar Diffuser Stability Monitor Performance”, IEEE Trans. Geosci. Remote Sens., 54, 631-639, 2016.
24. K. Lessel, S. McClain, “Low uncertainty measurements of 1149 bidirectional reflectance factor on the NPOESS/VIIRS solar 1150 diffuser”, Proc. SPIE, 6677, 66771O, 2007.
25. J. Sun, M. Chu, M. Wang, "Degradation nonuniformity in the solar diffuser bidiretional reflectance distribution function", Appl. Opt., 55, 6001-6016, 2016.
26. J. Sun, M. Wang, “Radiometric Calibration of the VIIRS Reflective Solar Bands with Robust Characterizations and Hybrid Calibration Coefficients”, Appl. Opt., 54, 9331-9342, 2015.
27. J. Sun, X. Xiong, and J. Butler, “NPP VIIRS on-orbit calibration and characterization using the moon”, Proceedings of SPIE- Earth Observing Systems XVII, vol. 8510, no. 85101I, 2012.

Figure Captions

Table 1. DNB EV sample versus aggregation mode. The aggregation modes are symmetric to nadir. The scan angles are relative to nadir.

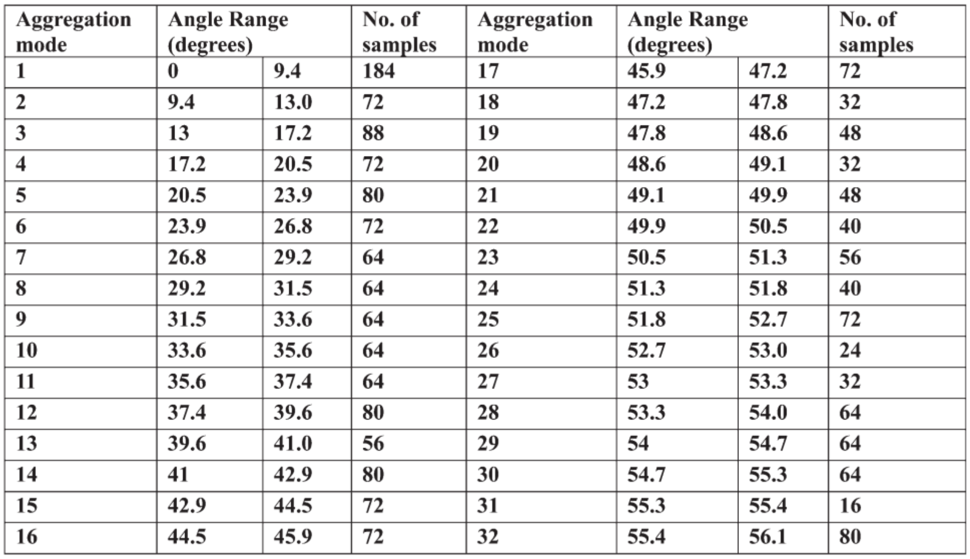

Aggregation mode	Angle Range (degrees)		No. of samples	Aggregation mode	Angle Range (degrees)		No. of samples
1	0	9.4	184	17	45.9	47.2	72
2	9.4	13.0	72	18	47.2	47.8	32
3	13	17.2	88	19	47.8	48.6	48
4	17.2	20.5	72	20	48.6	49.1	32
5	20.5	23.9	80	21	49.1	49.9	48
6	23.9	26.8	72	22	49.9	50.5	40
7	26.8	29.2	64	23	50.5	51.3	56
8	29.2	31.5	64	24	51.3	51.8	40
9	31.5	33.6	64	25	51.8	52.7	72
10	33.6	35.6	64	26	52.7	53.0	24
11	35.6	37.4	64	27	53	53.3	32
12	37.4	39.6	80	28	53.3	54.0	64
13	39.6	41.0	56	29	54	54.7	64
14	41	42.9	80	30	54.7	55.3	64
15	42.9	44.5	72	31	55.3	55.4	16
16	44.5	45.9	72	32	55.4	56.1	80

Table 2. Specification for SNPP VIIRS RSBs and SDSM detectors.

VIIRS Band	CW* (nm)	Band Gain	Detectors	Resolution*	SDSD Detector	CW* (nm)
M1	410	DG	16	742m x 776m	D1	412
M2	443	DG	16	742m x 776m	D2	450
M3	486	DG	16	742m x 776m	D3	488
M4	551	DG	16	742m x 776m	D4	555
I1	640	SG	32	371m x 387m	NA	NA
M5	671	DG	16	742m x 776m	D5	672
M6	745	SG	16	742m x 776m	D6	746
M7	862	DG	16	742m x 776m	D7	865
I2	862	SG	32	371m x 387m	D7	865
NA	NA	N	16		D8	935
M8	1238	SG	16	742m x 776m	NA	NA
M9	1378	SG	16	742m x 776m	NA	NA
M10	1610	SG	16	742m x 776m	NA	NA
I3	1610	SG	32	371m x 387m	NA	NA
M11	2250	SG	16	742m x 776m	NA	NA

*CW: Center Wavelength; DG: Dual Gain; SG: Singla Gain; Resolution: Track x Scan at Nadir after aggregation

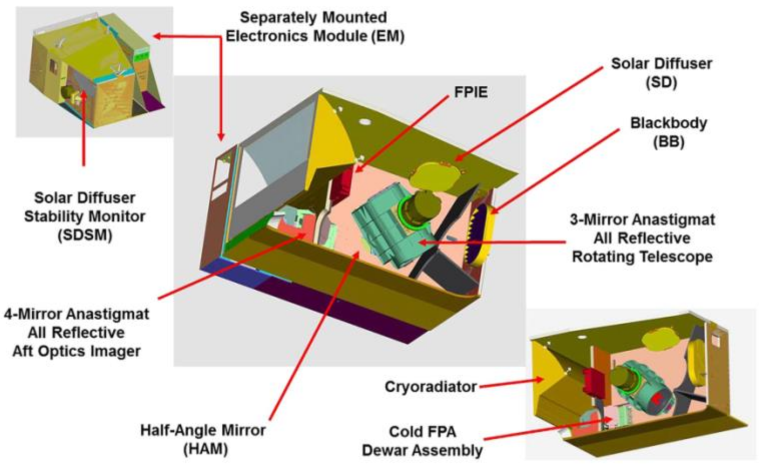

Figure 1. SNPP VIIRS Instrument and its on-board calibrators.

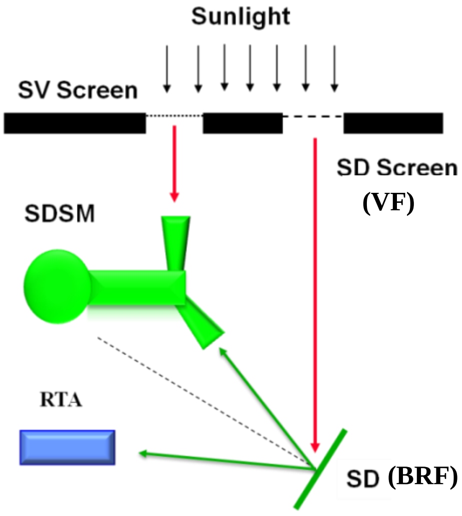

Figure 2. Schematic diagram for SD/SDSM calibration.

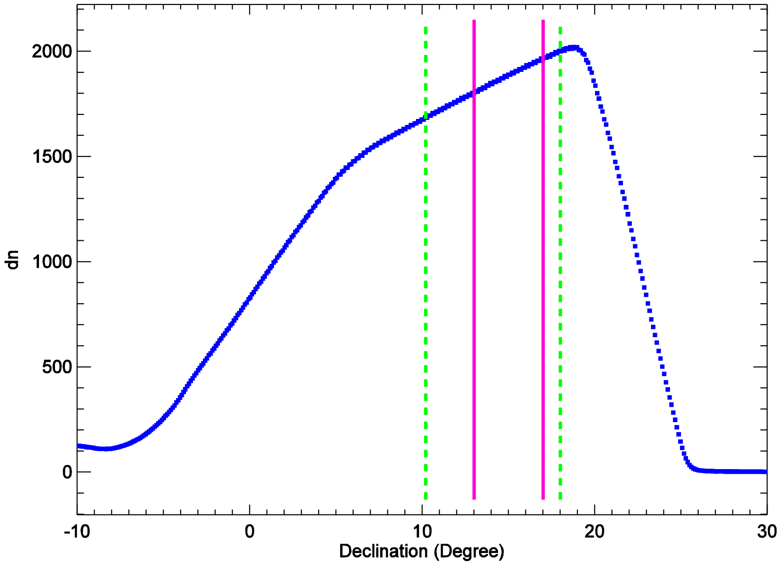

Figure 3. Background subtracted response of SNPP VIIRS band M6 detector 1 when it viewed SD on xxx x, 201x and the "sweet spot" for the RSBs viewing the SD. The two red vertical solid lines define the "sweet spot" used in the RSB SD calibration. The two green dashed lines define the "sweet spot" used for the DNB SD calibration in this analysis.

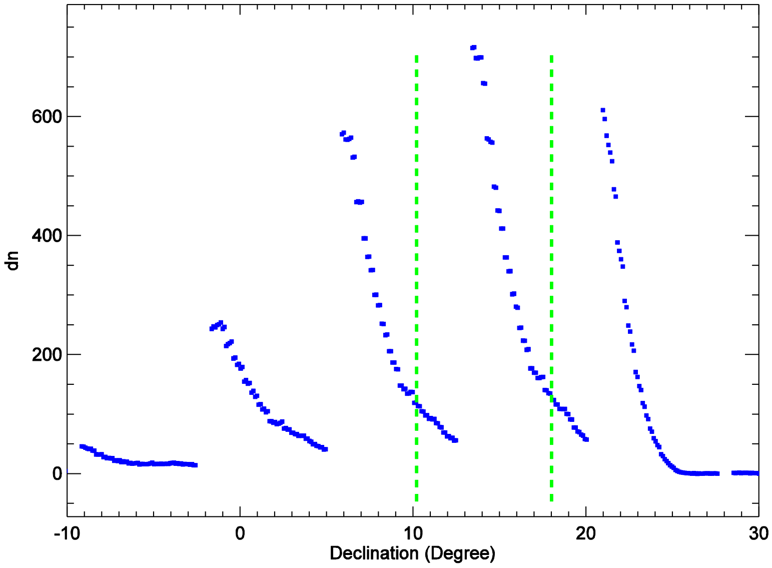

Figure 4. Background subtracted response of SNPP VIIRS DNB detector 1 when it viewed SD on xxx x, 201x.

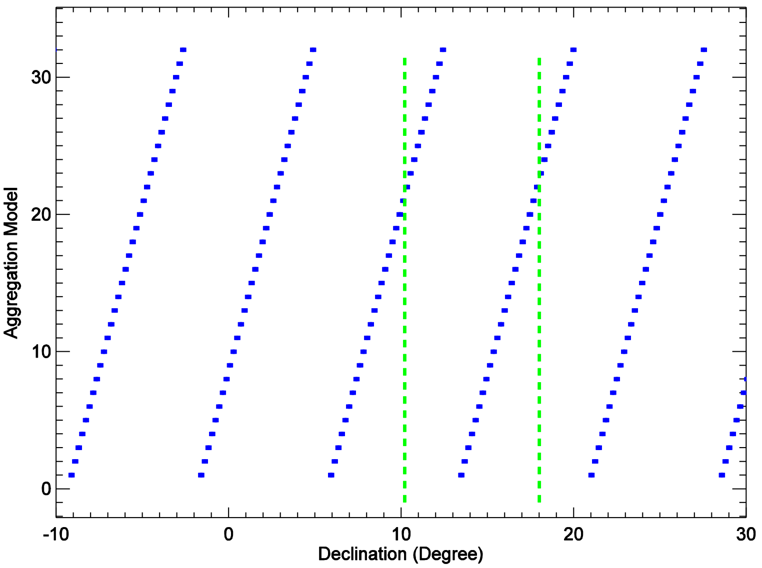

Figure 5. VIIRS DNB aggregation model for orbit xxxxx on xxx xx, 201x.

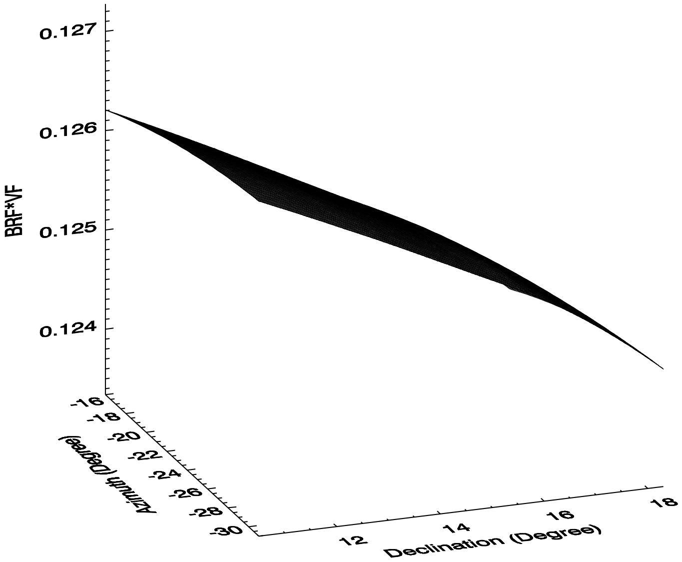

Figure 6. SNPP VIIRS band M6 BRF and VF product derived from the yaw measurements, which has been normalized to the prelaunch measured values.

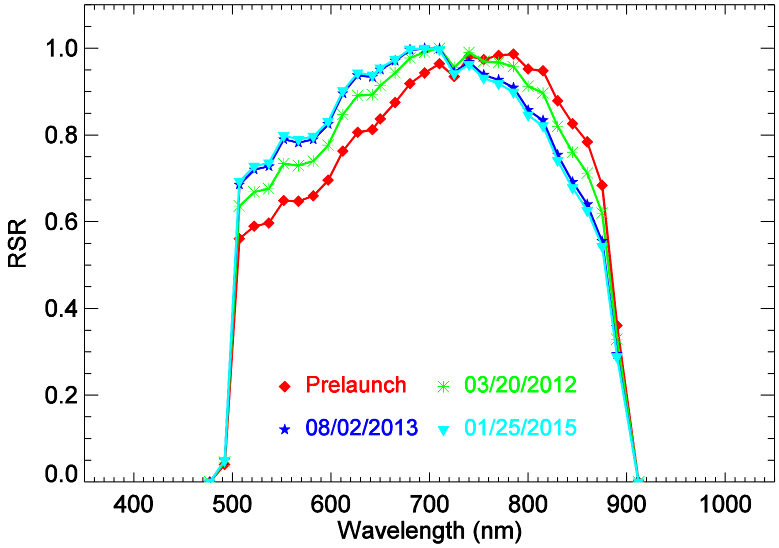

Figure 7. Time-dependent RSR for VIIRS DNB.

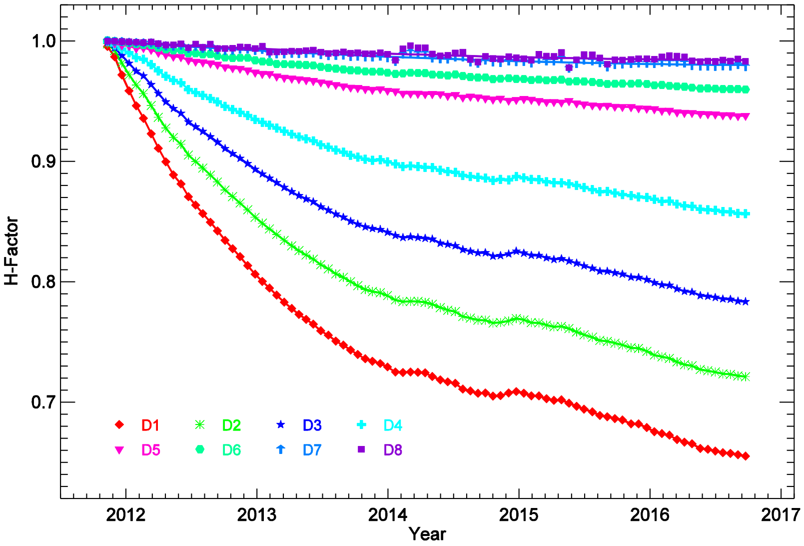

Figure 8. SD degradation derived from the SDSM measurements.

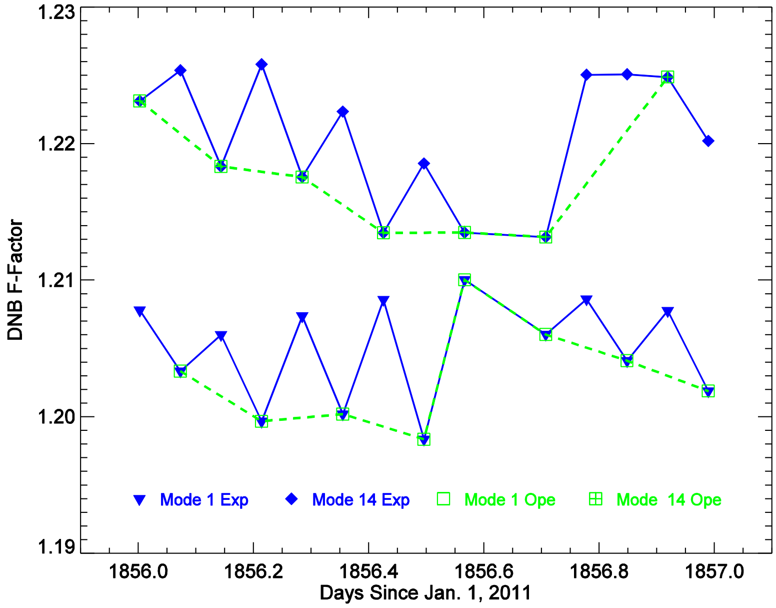

Figure 9. SNPP VIIRS DNB HAM side 1 detector 1 F-factors on February 1, 2016.

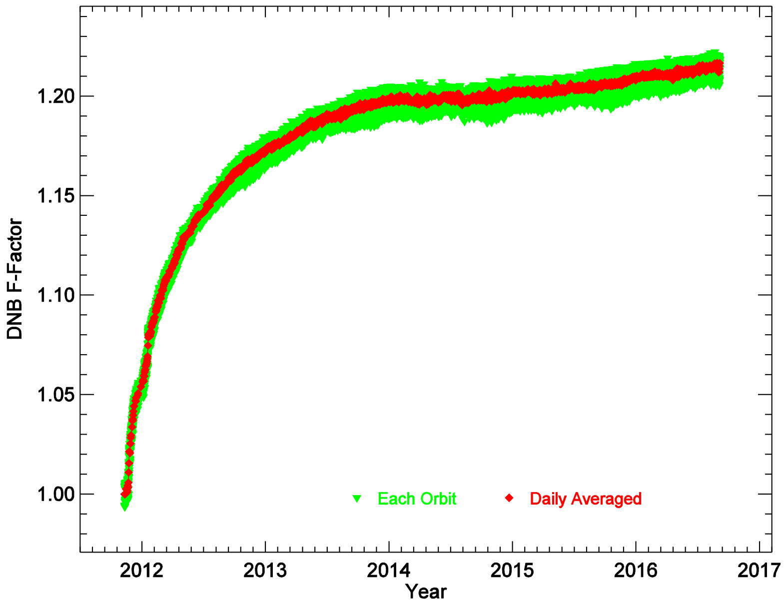

Figure 10. SNPP VIIRS DNB aggregation model 1 HAM side 1 detector 1 F-factors.

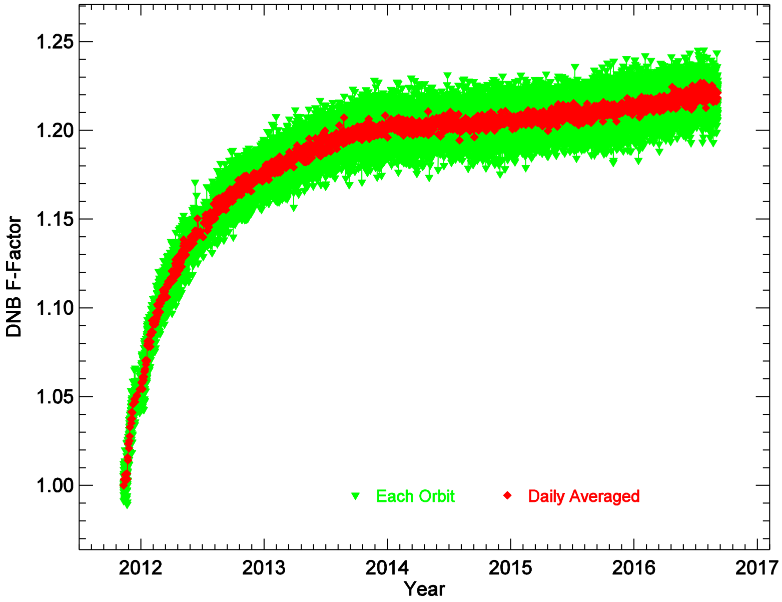

Figure 11. SNPP VIIRS DNB aggregation model 32 HAM side 1 detector 1 F-factors.

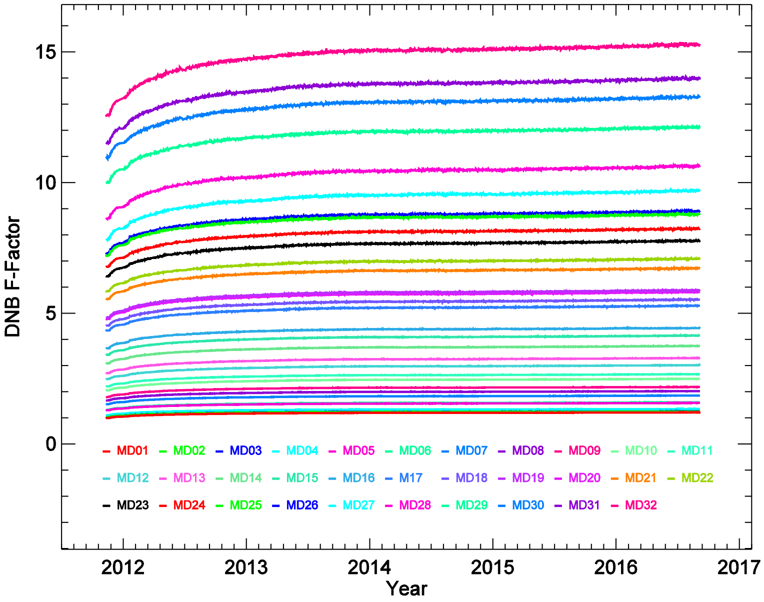

Figure 12. SNPP VIIRS DNB LGS HAM side 1 detector 1 F-factors normalized to first measured value of aggregation model (MD) 1 for all aggregation models.

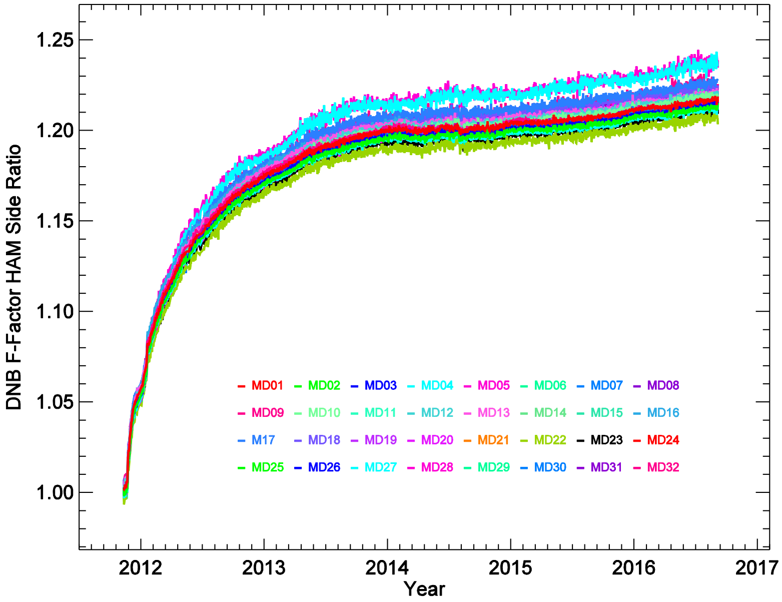

Figure 13. SNPP VIIRS DNB HAM side 1 detector 1 F-factors normalized to first measured values.

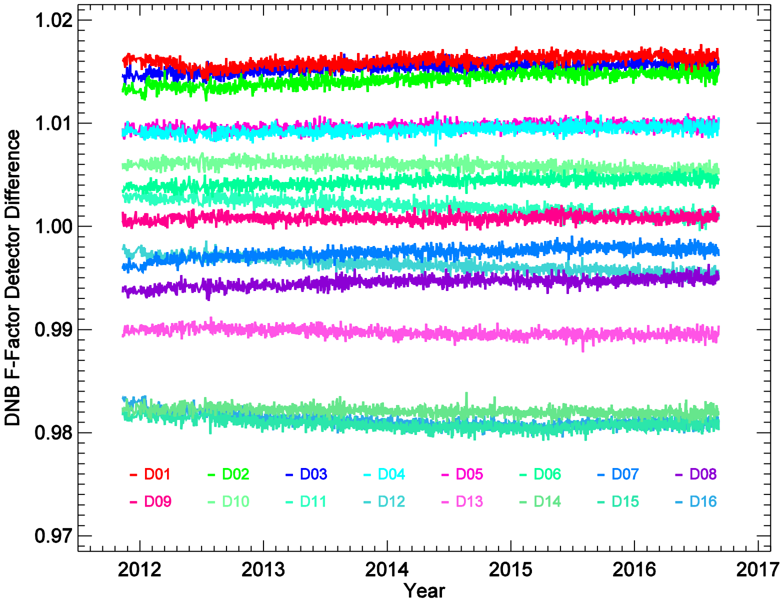

Figure 14. SNPP VIIRS HAM side 1 aggregation model 1 detector differences.

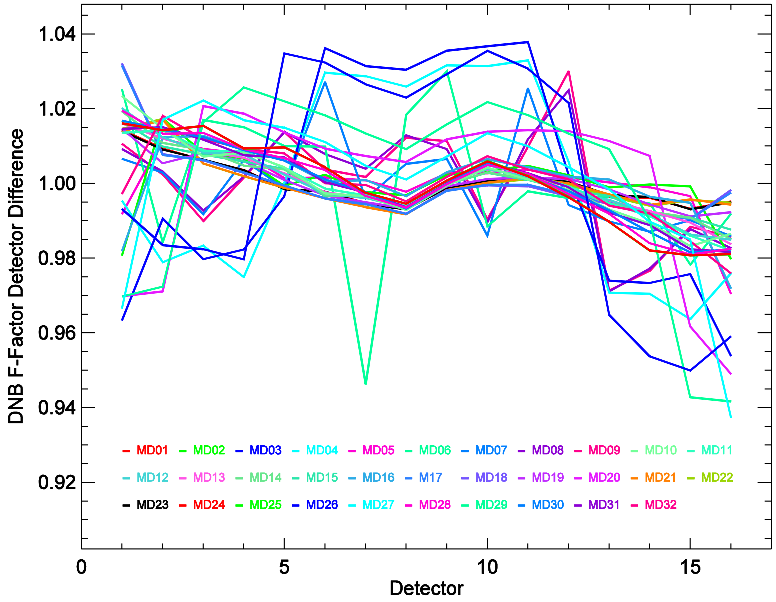

Figure 15. SNPP VIIRS DNB detector differences for all aggregation models.

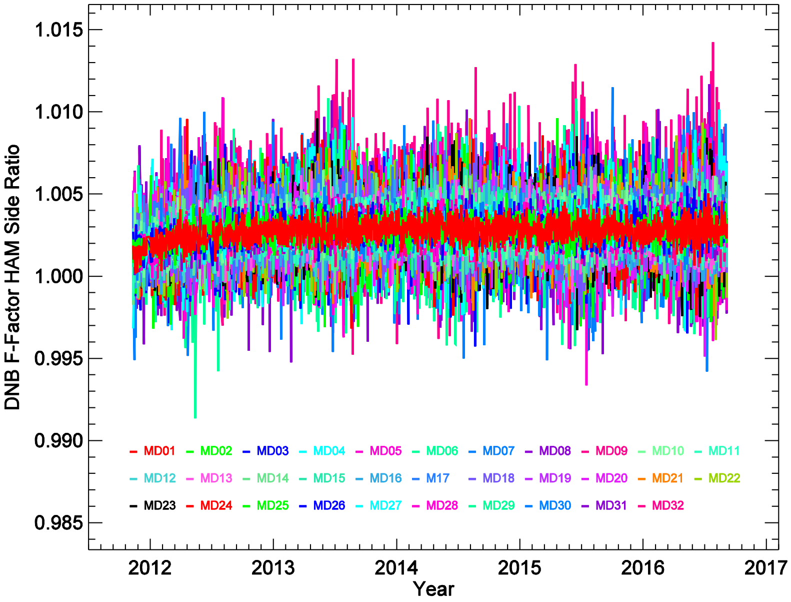

Figure 16. SNPP VIIRS DNB LGS F-factors HAM side ratios.

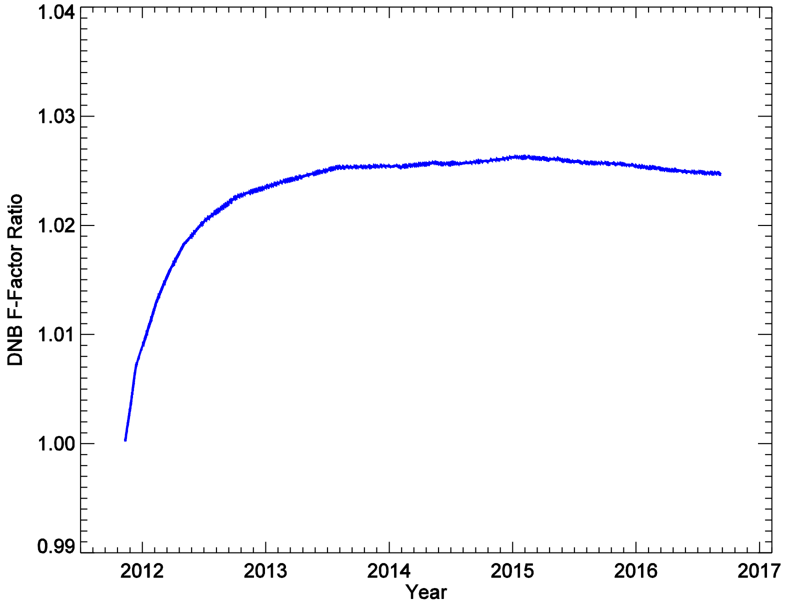

Figure 17. SNPP VIIRS DNB F-Factor ratios (with time-dependent RSR over prelaunch RSR).